CrossMark

# Impact of the Madden Julian Oscillation on the summer West African monsoon in AMIP simulations

Coumba Niang[1,2,3,4,5] · Elsa Mohino[3] · Amadou T. Gaye[1] · J. Bayo Omotosho[4]

**Abstract** At intraseasonal timescales, convection over West Africa is modulated by the Madden Julian Oscillation (MJO). In this work we investigate the simulation of such relationship by 11 state-of-the-art atmospheric general circulation models runs with prescribed observed sea surface temperatures. In general, the Atmospheric Model Intercomparison Project simulations show good skill in capturing the main characteristics of the summer MJO as well as its influence on convection and rainfall over West Africa. Most models simulate an eastward spatiotemporal propagation of enhanced and suppressed convection similar to the observed MJO, although their signal over West Africa is weaker in some models. In addition, the ensemble average of models' composites gives a better performance in reproducing the main features and timing of the MJO and its impact over West Africa. The influence on rainfall is well captured in both Sahel and Guinea regions thereby adequately producing the transition between positive and negative rainfall anomalies through the different phases as in the observations. Furthermore, the results show that a strong active convection phase is clearly associated with a stronger African Easterly Jet (AEJ) but the weak convective phase is associated with a much weaker AEJ. Our analysis of the equatorial waves suggests that the main impact over West Africa is established by the propagation of low-frequency waves within the MJO and Rossby spectral peaks. Results from the simulations confirm that it may be possible to predict anomalous convection over West Africa with a time lead of 15–20 day.

✉ Coumba Niang
niangcoumba@hotmail.fr

1    Laboratoire de Physique de l'Atmosphère et de l'Océan Siméon Fongang (LPAO-SF), Ecole Supérieure Polytechnique (ESP), Université Cheikh Anta Diop, BP 5085, Dakar-Fann, Senegal

2    Instituto de Geociencias (IGEO), Agencia Estatal Consejo Superior de Investigaciones Científicas CSIC, Madrid, Spain

3    Departamento de Física de la Tierra, Astronomia y Astrofisica I, Geofísica y Meteorologia, Universidad Complutense de Madrid (UCM), Madrid, Spain

4    WASCAL, Department of Meteorology, Federal University of Technology Akure, Ondo State, Nigeria

5    Instituto de Ciencias Matematicas, CSIC-UAM-UC3M-UCM, C/Nicolas Cabrera 15, Campus Cantoblanco UAM, 28049 Madrid, Spain

## 1 Introduction

The Madden Julian Oscillation is a tropical disturbance that propagates eastward around the tropics from the western Indian Ocean to the western Pacific Ocean with a periodicity of around 30–90 days (Madden and Julian 1971). This phenomenon was firstly identified by Madden and Julian (1971) by analysing zonal wind anomalies data from Canton Island. It is a large scale coupling between the atmospheric circulation and the tropical deep convection (Zhang 2005). Madden and Julian (1994) describe the MJO as the most dominant mode of intraseasonal variability over the tropical atmosphere. It has been estimated that one-half of tropical intraseasonal variance over the western Pacific is explained by the MJO (Hendon et al. 1999; Kessler 2001).

The MJO has a wide range of impacts, affecting precipitation and atmospheric circulation around the tropics and

subtropics (Yasunari 1979; Jones and Schemm 2000; Jones et al. 2004; Wheeler and McBride 2005; Zhang 2005; Donald et al. 2006). It also influences tropical cyclone activity in the eastern Pacific and Atlantic basins during the Northern Hemisphere summer (Liebmann et al. 1994; Maloney and Hartmann 2000; Ventrice et al. 2011). Furthermore, some studies have also highlighted a relationship between the MJO signal and heavy precipitation events over California, South Atlantic, Southwest Asia and also East Africa (Higgins et al. 2000; Jones et al. 2000; Bond and Vecchi 2003; Carvalho et al. 2004; Liebmann et al. 2004; Wheeler and Hendon 2004; Barlow et al. 2005).

The economy of West African countries is highly dependent on agricultural and water resources, which makes them highly vulnerable to rainfall variability, especially at intraseasonal time scales (Gadgil and Rao 2000; Sultan et al. 2005). The occurrence of wet and dry spells can significantly modulate the crop yield, which is a function of the repartition of rainfall during the season (Janicot and Sultan 2001). At these time scales, there are two main modes of variability over West Africa at 10–25 and 25–60 days (Janicot and Sultan 2001; Sultan et al. 2003; Mounier and Janicot 2004; Mounier et al. 2007). Rainfall variability in the 25–60 day range appears to have a MJO contribution since they share the same range of periodicity. Despite some works that suggested a weak or non-existence relation between the MJO and anomalous convection over West Africa (Knutson and Weickmann 1987; Maloney and Hartmann 2000), more recent studies point to a 20 days lag between enhanced convection over the Indian Ocean associated with the MJO and reduced convection over West Africa (Matthews 2004; Maloney and Shaman 2008; Janicot et al. 2009; Lavender and Matthews 2009; Pohl et al. 2009; Mohino et al. 2012).

Despite all the studies performed, the mechanisms through which MJO impacts West Africa is not clearly understood. Matthews (2004) and Maloney and Shaman (2008) suggest that eastward dry equatorial Kelvin and westward Rossby equatorial waves triggered by MJO activity over the warm pool can explain the impact of the MJO on West Africa. Lavender and Matthews (2009) show that locally reduced convection associated with latent heating anomalies over the warm pool that force dry equatorial westward Rossby and eastward Kelvin waves reach Africa approximately 20 days later. The studies of Janicot et al. (2009) and Mohino et al. (2012) highlight the role of convectively coupled Rossby waves in explaining the overall impact of the MJO on convection anomalies over West Africa.

GCMs still have problems to realistically represent the MJO signal (Slingo et al. 1996; Waliser et al. 2003; Lin et al. 2006; Zhang et al. 2006; Kim et al. 2009; CLIVAR 2009). The spectral analysis in the 30–70 day periodicity of 200 hPa velocity potential from atmosphere-only GCM simulations

shows the inability of models to properly simulate the observed spectral peak in the zonal wavenumber 1 (Slingo et al. 1996). In addition, Lin et al. (2006) examined Coupled Model Intercomparison Project phase 3 (CMIP3) models and found that only two models simulated a realistic variance and the main features of the MJO rainfall pattern. From the set of GCM models analysed by Kim et al. (2009) only two showed relatively better skill in representing the MJO. Recently, Hung et al. (2013) evaluated the MJO and convectively coupled equatorial waves using simulations from the Coupled Models Intercomparison Project phase 5 (CMIP5). Their results show that the CMIP5 models exhibit an overall improvement with respect to CMIP3 in simulating the tropical intraseasonal variability of rainfall with larger MJO variance. Crueger et al. (2013) performed a variety of uncoupled (AMIP-style) and coupled simulations with different grid resolutions. Their analysis suggests that atmosphere-only experiments show less MJO variability than coupled models (typically one-quarter and one-third of the variance found in reanalysis, respectively). However, they concluded that the air–sea coupling is not the most relevant factor for a good MJO simulation. In fact, Mauritsen et al. (2012) show that a robust MJO simulation is mainly related to the ability of a GCM to represent the moisture-stratiform instability process, low-level moisture convergence and discharge–recharge mechanism. Despite the numerous works devoted to the assessment of MJO simulation in coupled and uncoupled models, very few have evaluated the simulation of the MJO impact over West Africa. Such an evaluation can help improve our understanding of the mechanisms underlying the MJO-West Africa link and are also a first step to know if middle-range dynamical prediction of dry and wet spells over West Africa is feasible.

The aim of this paper is to evaluate the simulation of the impact of the MJO on rainfall and convection over West Africa and the dynamical mechanism involved in state-of-the-art models. For this aim, we use a set of Atmospheric Model Intercomparison Project (AMIP) simulations from models participating in CMIP5.

## 2 Data and methodology

In this study we focus on the extended summer season which is calculated from 1st May to 30th September in the period 1979–2008.

### 2.1 Data

#### 2.1.1 Observational datasets

Daily interpolated Outgoing Longwave Radiation (OLR) measured from National Oceanic and Atmospheric

**Table 1** Summary of models, their assigned numbers, number of integrations (number of years for each simulation multiplied by the number of ensemble members used), horizontal resolutions, convections schemes and the different institutes involved for the analysis

| Models | Assigned numbers | Number of integration | Lat × lon | Convect schemes | Institutes |
|---|---|---|---|---|---|
| BCC-CSM1-1 | 1 | 30 | 2.8° × 2.8° | Tongwen Wu (2012) | Beijing Climate Center, China Meteorological Administration |
| BCC-CSM1-1-M | 2 | 30 | 1.1° × 1.25° | Tongwen Wu (2012) | Beijing Climate Center, China Meteorological Administration |
| CMCC-CM | 3 | 30 × 3 | 0.75° × 0.75° | Tiedtke (1989)/Nordeng (1994) | Centro Euro-Mediterraneo per I Cambiamenti Climatici |
| CNRM-CM5 | 4 | 30 | 1.4° × 1.4° | Philippe Bougeault (1985) | Centre National de Recherches Meteorologiques |
| HadGEM2-A | 5 | 30 | 1.25° × 1.875° | Maidens and Derbyshire (2006) | Met Office Hadley Centre |
| IPSL-CM5A-LR | 6 | 30 × 6 | 1.875° × 3.75° | Emanuel (1991) | Institut Pierre-Simon Laplace |
| IPSL-CM5A-MR | 7 | 30 × 4 | 1.25° × 2.5° | Emanuel (1991–1993) | Institut Pierre-Simon Laplace |
| MPI-ESM-LR | 8 | 30 × 4 | 1.8° × 1.875° | Roeckner et al. (2003) | Max Planck Institute for Meteorology (MPI-M) |
| MPI-ESM-MR | 9 | 30 × 4 | 1.8° × 1.875° | Tiedtke (1989)/Nordeng (1994) | Max Planck Institute for Meteorology (MPI-M) |
| MRI-CGCM3 | 10 | 30 | 1.1° × 1.1° | Yukimoto et al. (2011) | Meteorological Research Institute |
| NorESM1-M | 11 | 30 × 3 | 1.9° × 2.5° | Bentsen et al. (2012) | Norwegian Climate Centre |

Administration (NOAA) is used as indicator of convection (Liebmann and Smith 1996) in the tropical region. It spans the period from mid-1974 to present and it has a horizontal resolution of 2.5°. The daily global rainfall data with a spatial resolution of 1° used in this study comes from GPCP data set and covers the period from 1997 to present (Huffman et al. 2001). For zonal winds, we use reanalysis data from ERA-Interim (Dee et al. 2011) to study the dynamics associated with the MJO and is used for the 1979–2008 period. All datasets used through the study are interpolated into a grid of 3° in longitude and 2° in latitude for a better comparison among all simulations.

### 2.1.2 Model simulations

In this study we use simulations carried out in the framework of the CMIP5 (Taylor et al. 2012) project. Among all the simulations, we focus on the AMIP experiment, which were performed by Atmosphere General Circulation Models, forced with prescribed sea surface temperatures (SST) variations in the 1979-present period. The basic purpose of AMIP simulations is to pledge the systematic intercomparison and validation of the performance of GCMs on intraseasonal timescale as well as to perform some models diagnostic under realistic conditions (Taylor et al. 2012).

An overview of the models with the ensemble members, convection schemes and horizontal resolutions of the simulations is provided in Table 1. The number of ensembles used differs from one model to another based on the availability of data during our study. For each model daily outgoing longwave radiation and zonal winds at 200 and 850 hPa are used to define the MJO index and also to study the dynamics related to it. The simulated rainfall is also used to estimate the impact of the MJO on West African rainfall variability.

### 2.2 Methodology

#### 2.2.1 Definition of the MJO cycle in observations

For this study the MJO cycle is analyzed using an approach similar to the one proposed by Wheeler and Hendon (2004). We firstly apply a 20–90 day band-pass filter to extract the periodicity related to the MJO signal, while removing as well the annual cycle and the interannual variability. Then standardized anomalies of zonal winds and OLR are computed and averaged over the tropics between 15°S and 15°N. A Combined Empirical Orthogonal Function (CEOF) analysis (Venegas 2001) is performed on the zonal winds at 850 and 200 hPa and OLR. The two leading CEOF modes are used to describe the MJO activity and to build composite maps that illustrate the progression of the MJO along the equator with a succession of enhanced and suppressed convection events. A two-dimensional phase diagram is built with the principal components (PCs) of the two leading CEOFs. Such phase diagram is further divided into eight sectors corresponding to the eight phases with which we describe the MJO cycle (Fig. 1d). All dates that lie in the same sector of the phase diagram are used to calculate composite maps for each phase of the cycle. Only those dates in which the MJO index exceeds a threshold of one standard deviation are used to build the composite
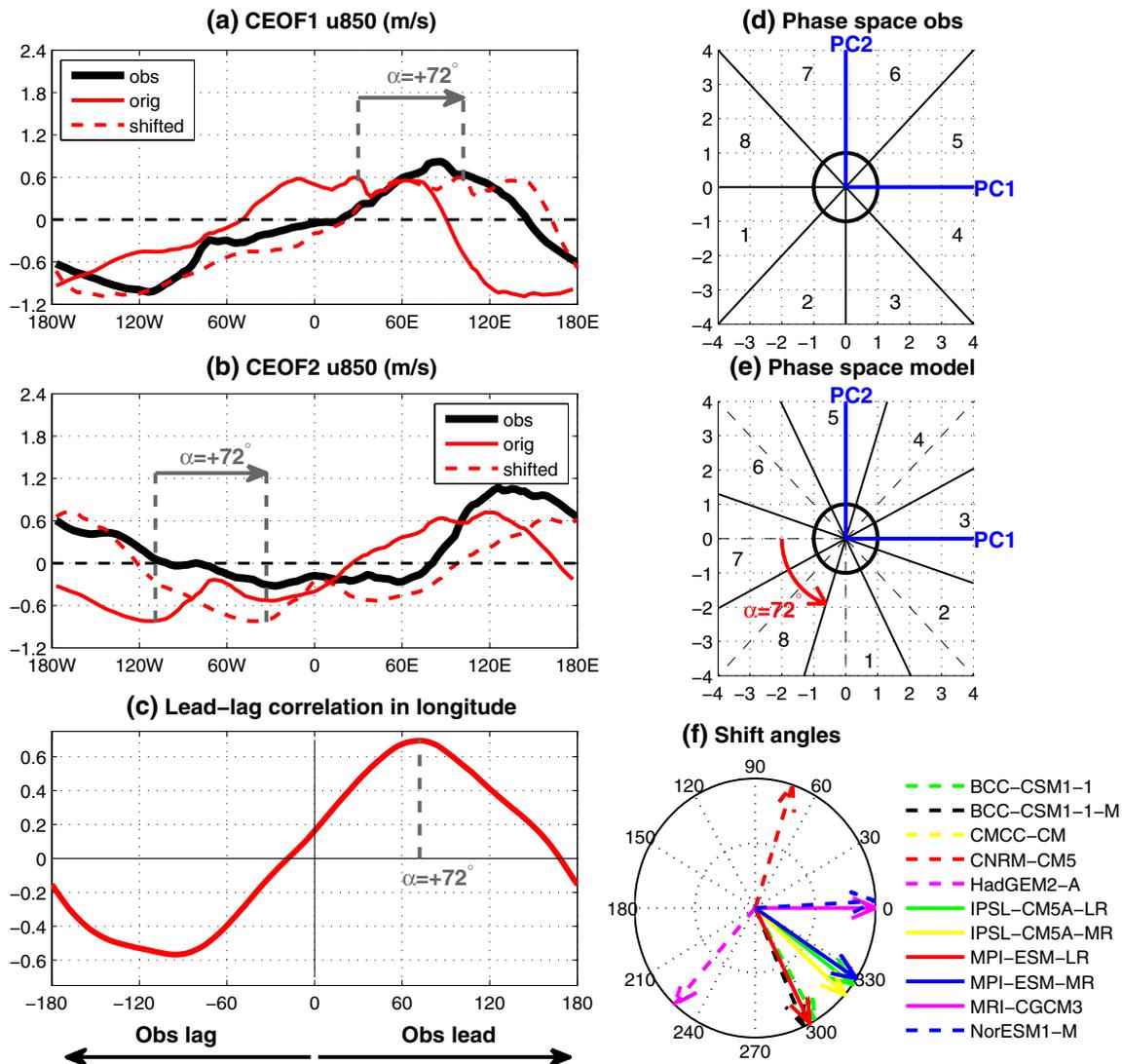
**(a) CEOF1 u850 (m/s)**

**(b) CEOF2 u850 (m/s)**

**(c) Lead–lag correlation in longitude**

**(d) Phase space obs**

**(e) Phase space model**

**(f) Shift angles**

**Fig. 1** Zonal wind anomalies at 850 hPa (m/s per standard deviation of the PC) corresponding to the first (**a**) and second (**b**) CEOF modes for the observations (*solid black line*) and CNRM-CM5 simulation (*solid red line*). The *red dashed line* shows the modelled pattern shifted by 72° in longitude. **c** Lead-lag correlation in longitude between the six CEOF patterns (three variables times two CEOF modes) for the observations and CNRM-CM5 model. The maximum correlation obtained at 72° east is highlighted in *grey*. **d** The eight

sectors in which the PC1-PC2 observed phase space is divided in order to build the composite maps. The *circle* shows the one standard deviation threshold used for the composite analysis. **e** The eight sectors in which the PC1-PC2 phase space from the CNRM-CM5 model is divided in order to build the composite maps. The *circle* shows the one standard deviation threshold used for the composite analysis. **f** Angles used to shift the CEOF patterns and the phase space for each model (see details in the *text*)

maps. A two-tailed *t* test is applied to evaluate the statistical significance of the composite maps.

To calculate the time it takes for the MJO to cover its cycle we first track the MJO evolution in the phase space and define an MJO event when at least four complete consecutive phases are covered by its evolution. We then divide the total number of days taken by that event by the number of complete phases crossed and we average over all events in all years and obtain the average time it takes for the MJO to cover a phase of its cycle.

### 2.2.2 Definition of the MJO cycle in simulations

For the simulations, the same procedure is followed to obtain the CEOF modes: we apply the same 20–90 day band-pass filter and we standardize anomalies and average them in the 15°S–15°N region. The anomalies from those models with ensemble runs are concatenated in time before the CEOF analysis. The two leading CEOF modes are used to describe the simulated MJO cycle (as it is shown in Sect. 3). However, for most models the CEOF patterns

obtained are shifted with respect to the observations. In Fig. 1, we show an example for the CNRM-CM5 model: the CEOF patterns for the zonal wind at 850 hPa of the two leading modes shows a structure similar to the one obtained from observations though shifted to the west (Fig. 1a, b). The model's results for the CEOF patterns of OLR and zonal wind at 200 hPa are consistent with this westward shift (not shown). Since the MJO patterns propagate eastwards, this means that the CNRM-CM5 CEOF patterns lag the observed ones. In order to better compare the CEOF patterns among models and with the observations, we shift the modelled ones in longitude towards the observed ones. To choose the best angle for the shift, we perform a lead-lag correlation in longitude between the observed CEOF patterns and the modelled ones (Fig. 1c). Note that all six CEOFs patterns (three variables times two CEOF modes) are concatenated together for this calculation. It consists of merging together the six CEOFs (fist two CEOFs of each of the three variable) side-by-side next to each other so that they can be treated as a single matrice. Then a lead lag correlation analysis of the three fields (OLR, U850 and U200) combined together is performed with respect to observations to determine the shift angle for each model. The longitude angle that maximizes the correlation is chosen to shift all CEOF patterns (Fig. 1a, b, dashed red curve). The shift angles differ from one model to another (Fig. 1f).

As with the observations, the Principal Components of the two leading CEOFs in each model are used to build a two-dimensional diagram. However, for those models that show a shift between their CEOF patterns and the observed ones, the definition of the MJO cycle based on dividing the PC phase space in the same eight sectors as in observations (Fig. 1d) leads to a shift in the modelled MJO cycle with respect to the observed ones. This is expected since those dates in the models when PC1 (PC2) are strong, show anomalies mostly related to CEOF1 (CEOF2) in the models, which are shifted in longitude with respect to observations.

The composite approach we use for observations assumes an ideal MJO cycle, in which anomalies propagate eastward as the MJO describes a circumference in the phase space travelling anticlockwise. In such a model, the MJO anomalies go round the planet (propagate 360° east in longitude until they return back to the origin) in the time it takes to go 360° round the phase space. If we suppose a uniform speed for the MJO anomalies to travel the cycle, a shift of α in longitude can be directly translated to a shift in α in the phase space. With this in mind and in order to better compare the MJO cycle among models and with the observations, we divide the phase space for the models into 8 sectors that are shifted with respect to the observations with the same angle as the one used to shift the CEOF patterns (Fig. 1e). The MJO cycle for each model is then

obtained as a composite map using all the dates that lie in the given sector. As with the observations, we use the 1 standard deviation threshold for the composite map and a two-tailed $t$ test to estimate its statistical significance. The average time for an MJO event to cover a complete phase of its cycle in the simulations is estimated in the same way as in the observations.

### 2.2.3 Wavenumber–frequency analysis and filtering

To investigate the roles of convectively coupled equatorial waves in the impact of the MJO on anomalous convection over West Africa, a wavenumber frequency spectral analysis has been performed on OLR (Wheeler and Kiladis 1999). This method is mainly used to diagnose the MJO (Wang and Schlesinger 1999; Wheeler and Kiladis 1999). Such method consists of separating the original OLR field into its symmetric and antisymmetric components with respect to the equator. The mean and linear trends of the deseasonalized OLR are removed in time and the ends of the series are tapered to zero. Fast Fourier Transforms (FFT) is performed first in longitude and then in time to obtain the wavenumber–frequency spectrum for each latitude. The OLR power is finally averaged over time segments and further summed over the 15°S–15°N latitude area. Hence, the strength of the different atmospheric waves in a signal can be highlighted in a wavenumber–frequency diagram for eastward and westward propagating waves (Hayashi 1982). In this work we focus on the symmetric OLR wavenumber–frequency spectra to look for convectively coupled equatorial waves.

Once the main waves are detected, the propagation of each of these waves is further analysed. We filter a given field taking only the wavenumber–frequency spectral content in certain domains corresponding to particular waves. Then, the composite analysis is repeated with this filtered field in the same way as explained above. Such approach allows us to show the propagation associated to each convectively coupled equatorial waves separately.

## 3 Results and discussions

### 3.1 Evolution of summer MJO through AMIP simulations

#### 3.1.1 CEOF analysis

The observed and simulated spatial structure of the two leading CEOF modes of OLR and zonal winds at 850 and 200 hPa as a function of longitude is shown in Fig. 2. Note that for better comparison, the simulated patterns have been shifted in longitude by the angles given in Fig. 1f.
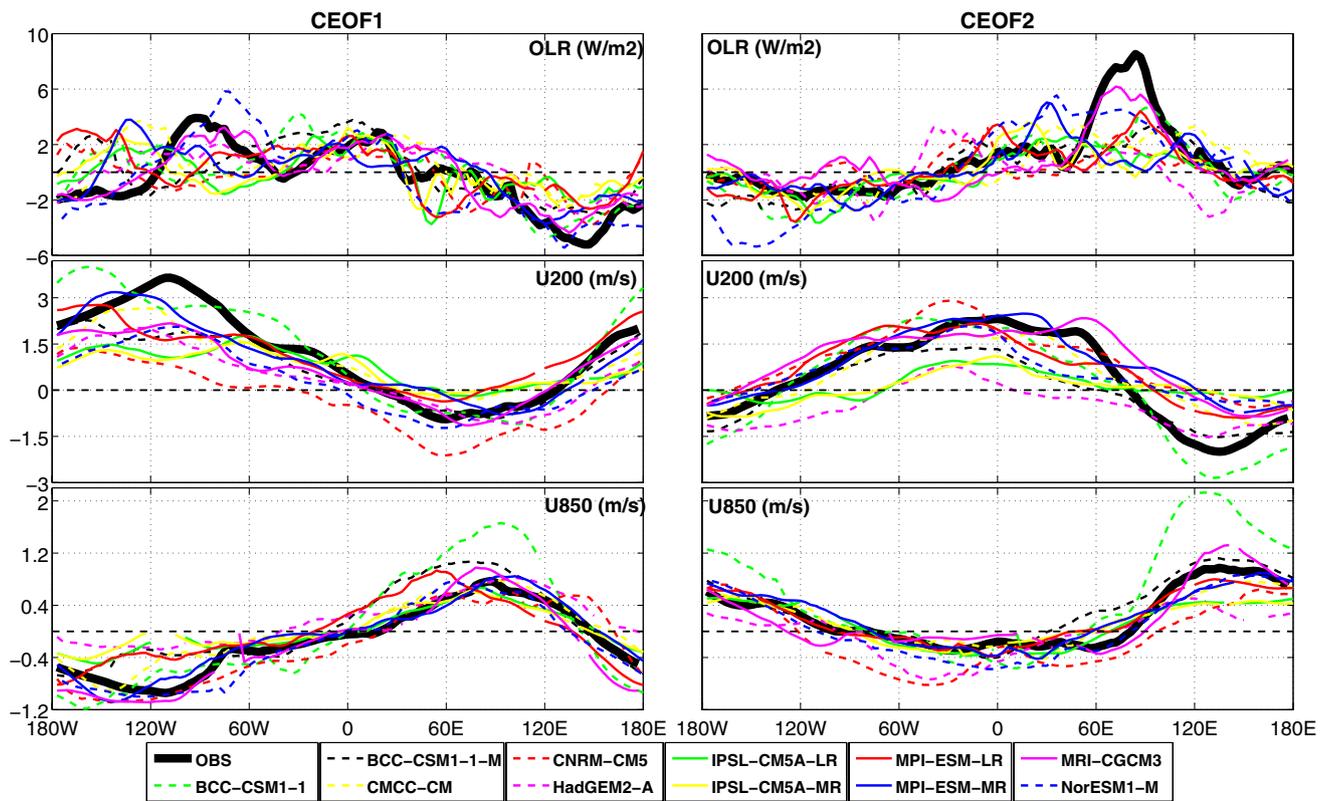
**Fig. 2** Observed (*thick black line*) and simulated first two CEOFs of summer OLR and zonal wind at 850 and 200 hPa anomalies from AMIP simulations. The *first line of figures* represent OLR, the *second one* the zonal wind at 200 hPa and the *last one* the zonal wind at 850 hPa anomalies. The units are W/m$^2$ per standard deviation of the associated first two CEOFs for OLR and m/s per standard deviation for zonal wind

The pattern of the first two CEOFs from the observations represents the main modes of variability over the tropics. These modes explain 22.1 and 15.5 % of the total observed variance of the filtered field during the summer period, respectively (Table 2). The explained variance of the first two CEOFs is underestimated by all the models (Table 2). The models NorESM1-M, BCC-CSM1-1 and CNRM-CM5 show better performance with values ranging from 14.8 to 17.9 % for CEOF1 and 13.8 to 14.7 % for CEOF2. The CEOF modes from the IPSL-CM5A-LR and IPSL-CM5A-MR show the least explained variance with 10.3 and 10.6 % for CEOF1 and 7.4 and 7.8 % for CEOF2. The first two CEOF modes are well separated from the third one in all models, according to the North et al. (1982) criterion.

The observed CEOF1 of OLR shows a pattern characterized by an enhanced convection over the maritime continent and a decreased one over central Africa and the East Pacific Ocean, while the second one exhibits a minimum of convection over the Indian Ocean. Regarding the simulations, there is some disparities in the OLR patterns among the models compared with the observations. For CEOF1, models are capable of simulating the observed maximum convection over the Maritime Continent, though with a

weaker magnitude. However, the simulation of the maximum of observed OLR (minimum convection) located over the Eastern Pacific shows much larger spread in terms of magnitude and location: the MPI-ESM-LR, IPSL-CM5A-LR, MPI-ESM-MR models shift this OLR maxima towards the west, whereas the NorEM1-M model simulates it more eastward with stronger anomalies. For the OLR maximum over Africa, models show a more consistent behaviour among themselves and with the observations. Regarding CEOF2, simulations tend to bring out enhanced convection over the Pacific Ocean and decreased convection over the Indian Ocean, in agreement with the observations. However, this last maximum of OLR is completely missed by the IPSL-CM5A-LR, IPSL-CM5A-MR and CNRM-CM models.

The zonal wind anomalies associated with the first two CEOFs in all models show a structure close to the observed one (Fig. 2). At low (high) levels the first CEOF component shows a maximum (minimum) of zonal wind anomalies over the Indian Ocean while the minimum (maximum) is located across the Pacific basin. CEOF2 of zonal wind shows a pattern similar to CEOF1 but shifted 60° to 120° to the east. The BCC-CSM1-1 tends to overestimate wind

anomalies, whereas the IPSL-CM5A-MR model tends to underestimate them with regards to the observations.

Compared to the observations, models show better performance in simulating zonal wind anomalies at low and high levels associated with the first two CEOFs than OLR anomalies. We speculate that such a poor performance and disparity among models in simulating OLR anomalies could be related to the different convection schemes used by them (Table 1). Some of the most important physical processes such as convection and cloud formation are represented through parametrisations. Randall et al. (2007) and Guilyardi et al. (2009) show that large systematic errors in climate simulations come mainly from the cloud parameterization used by the models.

The two first observed CEOF modes are not independent. Their lead-lag correlation shows that CEOF1 leads

**Table 2** Explained variance of the first two CEOFs of filtered data and the inverse of phase speed of the MJO cycle from the observations and simulations

| Models | CEOF1 (%) | CEOF2 (%) | Inverse of phase speed (days per phase) |
|---|---|---|---|
| NOAA/ERA-Interim | 22.1 | 15.5 | 4.8 |
| BCC-CSM1-1 | 17.9 | 14.7 | 4.7 |
| BCC-CSM1-1-M | 15.0 | 12.6 | 4.3 |
| CMCC-CM | 12.6 | 10.5 | 4.5 |
| CNRM-CM5 | 14.8 | 14.2 | 4.8 |
| HadGEM2-A | 11.5 | 9.0 | 4.7 |
| IPSL-CM5A-LR | 10.3 | 7.4 | 4.6 |
| IPSL-CM5A-MR | 10.6 | 7.8 | 4.9 |
| MPI-ESM-LR | 12.7 | 10.3 | 4.8 |
| MPI-ESM-MR | 13.2 | 10.9 | 4.6 |
| MRI-CGCM3 | 15.7 | 12.2 | 4.9 |
| NorESM1-M | 17.3 | 13.8 | 4.3 |

CEOF2 (Fig. 3). In accordance with Wheeler and Hendon (2004) such result suggests an eastward propagation of the convection and wind anomalies shown in Fig. 2 and can be used to capture the summer MJO. For the observations, the maximum correlation of 0.75 is obtained at a lag of 9 days. Regarding the simulations, models show a maximum of correlation ranging from 0.40 to 0.75 with a time lag of between 7 and 10 days. All models agree among themselves and with the observations in the eastward propagation of the convection and the wind anomalies shown in Fig. 2, because they either show that PC1 leads PC2 (MPI-ESM-LR, MPI-ESM-MR, MRI-CGCM3, BCC-CSM1-1, BCC-CSM1-1-M and CMCC-CM), or that minus PC2 leads PC1 (IPSL-CM5A-LR, IPSL-CM5A-MR, CNRM-CM5 and HadGEM2-A models). Such results also suggest that in the models the first two CEOFs are capturing the summer MJO and can be use to build the MJO cycle.

### 3.1.2 MJO composite cycle

To further analyse the simulation of intraseasonnal variability associated with the MJO, in Fig. 4 we show the composites of the deseasonalized OLR anomalies throughout the eight phases of the MJO cycle for the observations and the ensemble average of AMIP simulations. The ensemble mean is computed by averaging the composites maps of all individual simulations. For the observations, at phase 1 there are negative OLR anomalies centered over the Indian Ocean and positive ones over the western Pacific. The negative anomalies strengthen at phase 2 and move northward over the Indian Continent and eastward along the equator from phase 3–5. At phase 6 the anomalous negative OLR dissipates over the maritime continent and extends over the Pacific basin. Positive OLR anomalies develop over the Indian Ocean at phase 5 which brings out the transition from the active to the suppressed convection moving to

**Fig. 3** Lead-lag correlations between the principal components associated with the first and second CEOF from observation and AMIP simulations. The *x-axis* of this figure is in days while the *y-axis* represents the lead-lag correlation coefficients between PC1 and PC2
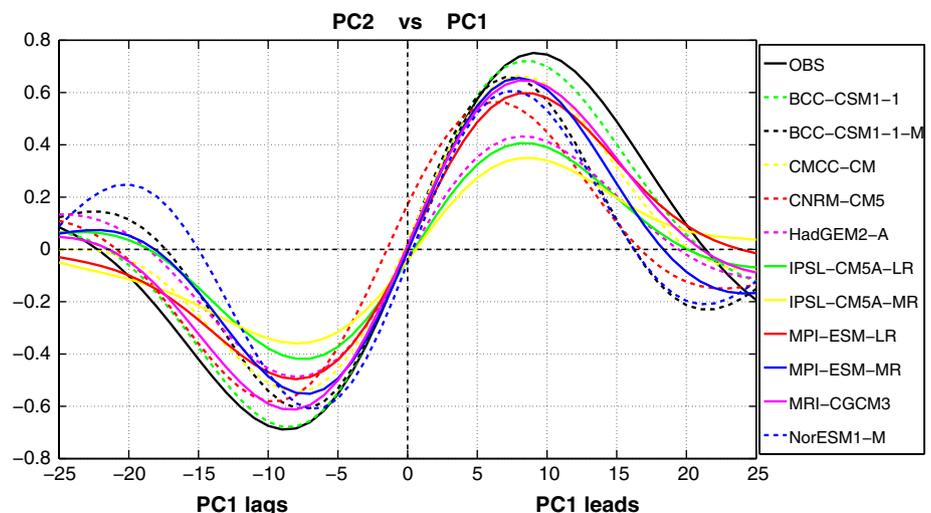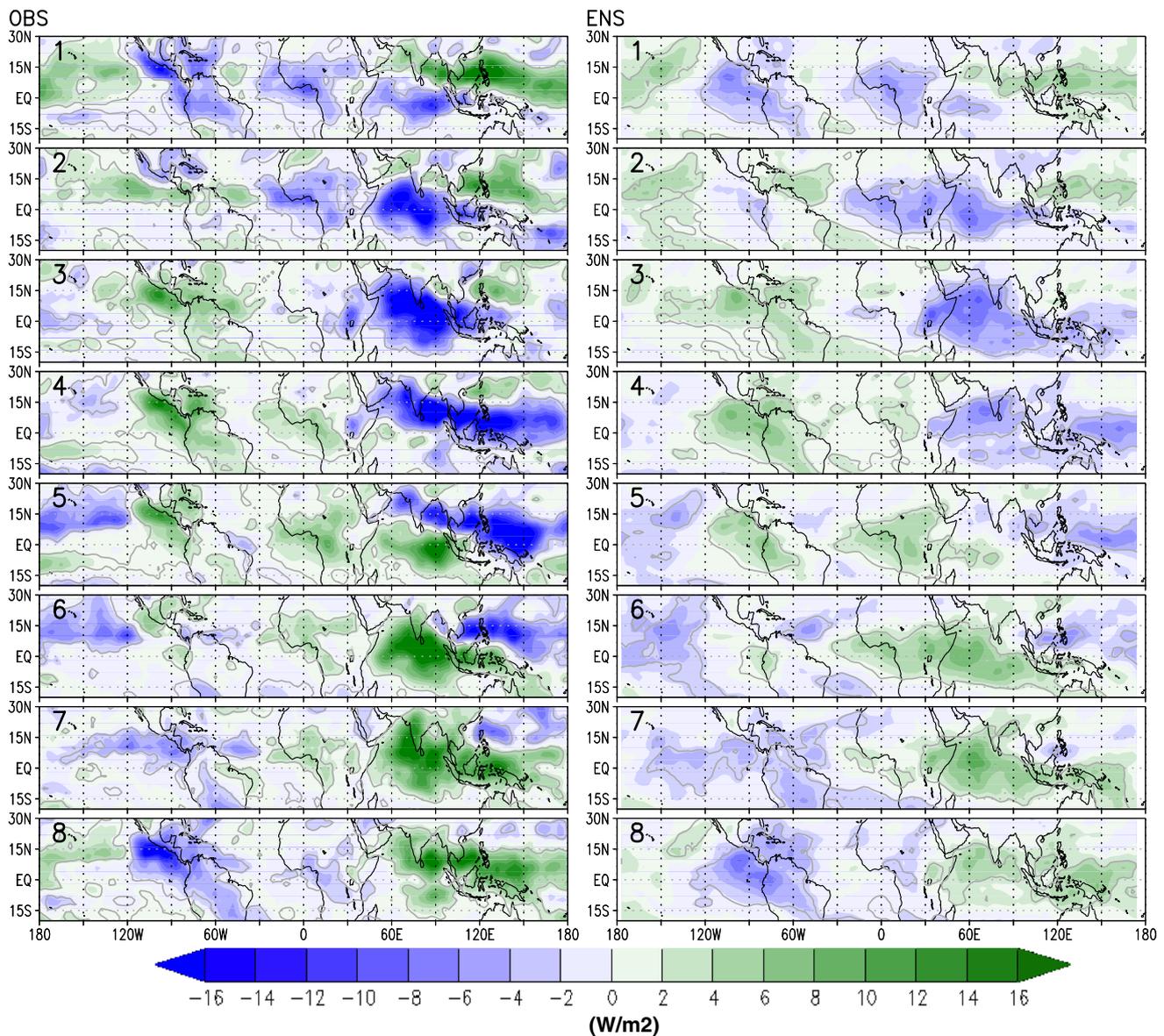
**Fig. 4** Summer composites of deseasonalized anomalies of OLR according to the eight phases associated with the MJO, from observations (*left*) and the ensemble average of AMIP composites (Figs. S1–S6; right). The ensemble composite is obtained as the average of the 11 models composites, which are previously phase-adjusted (see Sect. 2.2.2 for details). The units are W/m$^2$. The *grey contours* represent the 95 % significant regions obtained from a two-tailed *t* test

the central and eastern Pacific from phase 6–1. The ensemble average of AMIP simulations captures a clear eastward propagating signal in phase with the observed one, though with a weaker magnitude. Over the Indian Ocean the models locate the events of strong and weak convection more southward with respect to the observations and, although they simulate a northward propagation into the Indian continent, it does not penetrate further than north India.

In addition each of the models taken individually captures reasonably well the observed features of the eastward propagation of the MJO signal (Figure S1–S6).

Some models like the IPSL-CM5A-LR, IPSL-CM5A-MR, HadGEM2-A, CNRM-CM5 and CMCC-CM show a weak convective signal in terms of the evolution and the amplitude and simulate an eastward propagation less coherent with regards to the observations. The northward propagation over the Indian Ocean is not clearly highlighted in most of these models and is slower compared to the observations.

The spatial correlation between the observed and modelled tropical (15°S–15°N) OLR patterns are shown in Fig. 5a. The correlations show strong and significant values
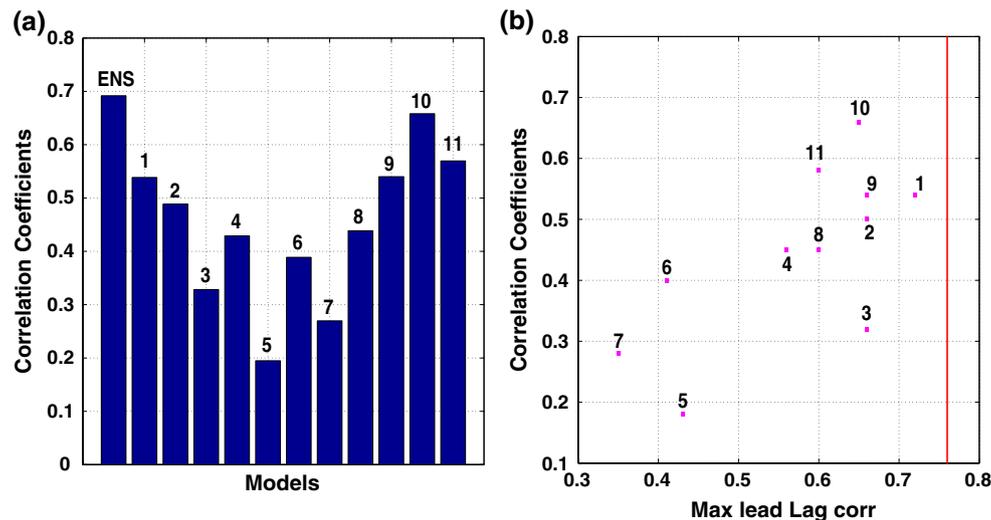
**Fig. 5** **a** Correlations of summer composites of deseasonalized OLR anomalies between the observations, individual simulations and the ensemble average of AMIP composites in the tropics (15°S–15°N). **b** Scatterplot between the maximum lead lag correlation of the first two principal Components (PC1 and PC2) and the correlation coef- ficients between the observations and each of AMIP's models in the tropics presented in plot **a**. The *red line* in **b** delimits the observed maximum lead lag correlation value. For convenience numbers are associated to the different models used through this study (see Table 1)

above 0.4 for most of the models (ENS, BCC-CSM1-1, BCC-CSM1-1-M, CNRM-CM5, IPSL-CM5A-LR, MPI-ESM-LR, MPI-ESM-MR, MRI-CGCM3 and NorESM1-M). CMCC-CM and IPSL-CM5A-MR simulated correlations ranging between 0.2 and 0.4 while it drops below 0.2 for HadGEM2-A model. Most of those models with higher pattern correlation with respect to the observations tend also to be those that show a stronger lead-lag correlation between the Principal Components of CEOF1 and CEOF2 (Fig. 5b). The MJO signal in the simulations tends to propagate faster than in the observations (it takes them roughly 4.3–4.8 days to cover each phase compared to the 4.8 days per phase in the observations) except for the MRI-CGCM3 and IPSL-CM5A-MR models, which show a slower propagation (approximately 4.9 days per phase) (Table 2).

In brief 5 out of the 11 models (NorESM1-M, MRI-CGCM3, BCC-CSM1-1, BCC-CSM1-1-M and MPI-ESM-MR) used are in good agreement with the observations in representing the main features of the evolution and propagation of the MJO pattern (correlation of the composites). A wide spread disagreement has also been noticed in the rest of the models which mainly simulated a weaker MJO signal with less coherency in the eastward propagation of the signal.

## 3.2 Impacts of MJO over West Africa

Over West Africa, the observations show strong negative OLR anomalies (enhanced convection) during phases 1 and 2, and strong positive ones (reduced convection) during phases 4 and 5 (Fig. 4). In average, the models reproduce the timing of the enhanced convection but shift to phases 5 and 6 the main positive OLR anomalies over West Africa (Fig. 4). To analyze the performance of individual models, in Fig. 6 we show the OLR composite maps over West Africa for all models in phases 1 and 5 as representative of the strong and weak convection phases over the region, respectively. Regarding the phasing, models agree with the observations with intense negative OLR anomalies during phase 1 and strong positive ones during phase 5 (Fig. 6). The main exception is the MRI-CGCM3 model, which shows very weak positive anomalies simulated over West Africa and an inconsistent pattern in phase 5 (Fig. 6). Regarding the pattern, the multi-model mean of composites shows OLR anomalies consistent with the observed ones in both phases. However, the individual models show more discrepancies (Fig. 6): the main positive and negative anomalies are shown south of 10°N in the IPSL-CM5A-LR and MPI-ESM-MR models. For some models, the magnitude of the OLR anomalies over West Africa is underestimated (e.g. IPSL-CM5A-MR, CMCC-CM models).

The MJO signal also shows an impact on rainfall over West Africa. In Fig. 7, we present the spatial distribution of rainfall composites for the observations (top) and the ensemble average of AMIP simulations (bottom) during the phases with the strongest and weakest observed MJO impact over West African convection (phases 1 and 5, respectively). The impact of the summer MJO on rainfall over West Africa is stronger during the strong convective phase of the MJO signal (above 2 mm/day in some
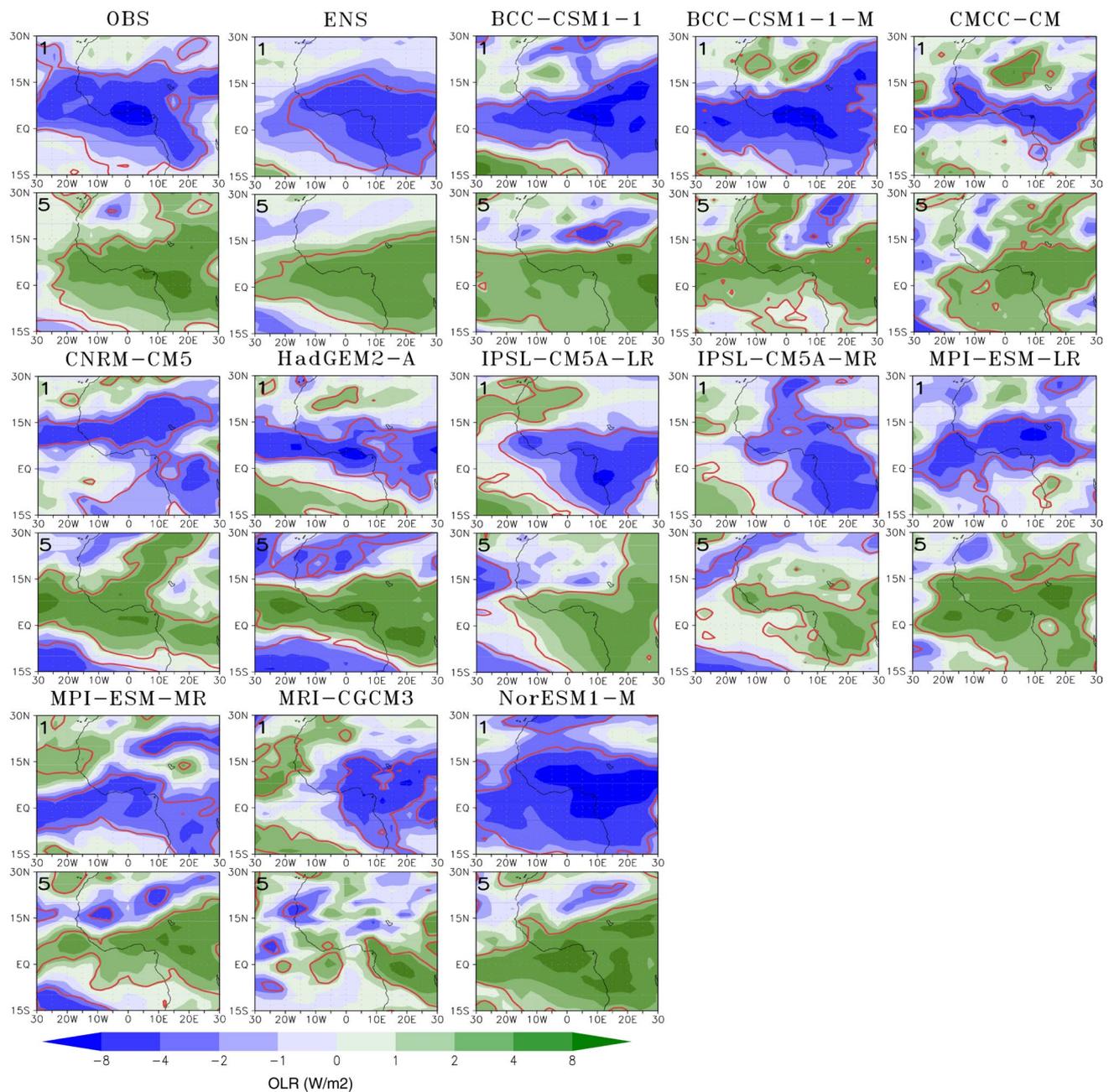
**Fig. 6** Summer composites of observed deseasonalized anomalies of OLR (W/m²) over West Africa during the strong (*1*) and weak (*5*) convective phases of MJO from the observations, individual AMIP simulations and the ensemble average of models' composites. *Red lines* represent the 95 % significant regions obtained from a two-tailed *t* test

locations) than during the weak convection phase. The maximum positive and negative rainfall anomalies during phases 1 and 5 are located over the Gulf of Guinea (Fig. 7) and propagate northwards during phase 2 and 5, respectively (not shown). The ensemble average of models' composites underestimates rainfall anomalies in both phases (Fig. 7), which could be related to the averaging of model outputs. It shows a higher impact of the MJO in the strong convection phase over the continental areas, where there

is a high consistency among the models in the sign of the anomalies (especially over Nigerian and Cameroon highland and over the Northeast of Soudanian zone) (Fig. 7). In the weak convection phase over West Africa, models agree among themselves and with the observations showing the main rainfall anomalies over the Gulf of Guinea.

To evaluate the timing of the rainfall anomalies simulated over West Africa by the individual models, in Fig. 8 we present the observed and simulated composites of rainfall

**Fig. 7** Composites of rainfall anomalies (mm/day) during the MJO strong (**a, c**) and weak (**b, d**) convective phases over West Africa for the observations (**a, b**) and the ensemble average of models' composites (**c, d**). The crosses mark the areas where at least eight (8) out of 11 models are consistent on the sign of the composite. Grey contours represent the area where rainfall anomalies are 95 % significant according to a two-tailed t test
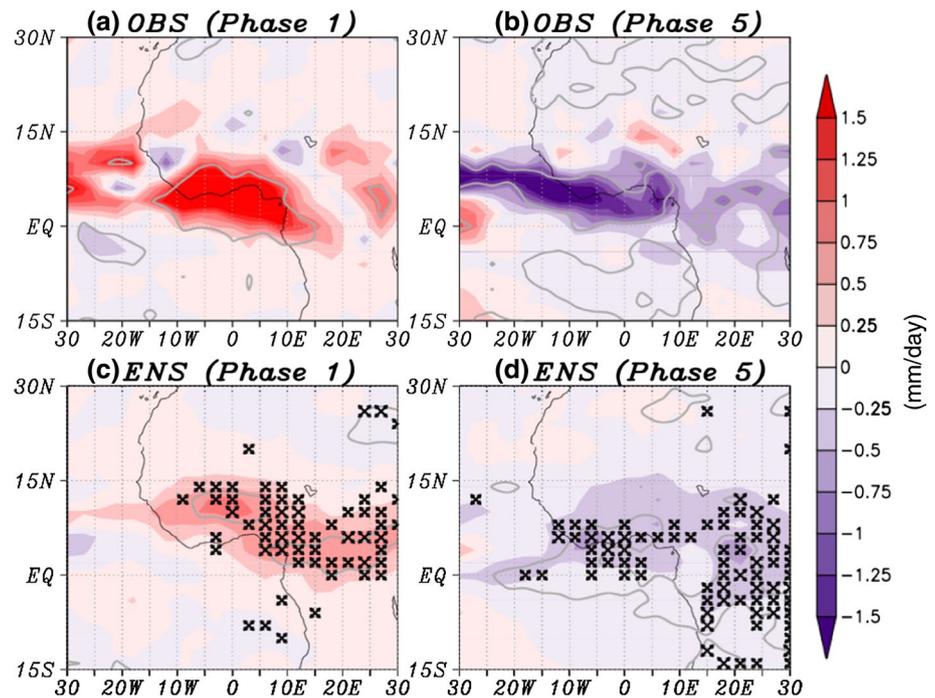


averaged over West Sahel (20°W–10°E and 10°N–20°N) and Guinean zone (12°W–6°E and 4°N–7°N) respectively. For the observations, over West Sahel, the phases 1, 2, 3, 7 and 8 are associated with wet conditions while drier conditions occur during phases 4, 5 and 6. The transition phase of the MJO from negative to positive rainfall anomalies is well marked in the observed rainfall composites in both regions though it occurs one phase later over Guinean zone than over the West Sahel (between phases 7–8 and 6 and 7, respectively). The timing of the MJO impact on rainfall is well captured by the models: most of them simulate positive (negative) rainfall anomalies over both regions during phases 1 and 2 (5 and 6). While rainfall anomalies over Guinea are underestimated by all models, those over the West Sahel are overestimated by the CNRM-CM5 and NorESM1-M models.

The impact of the MJO on the AEJ during the strong and weak convective phases is presented in Fig. 9. In phase 1 which corresponds to the strong convective phase, the AEJ is extended to the east. Such result suggests that the strong active convection is associated with the AEJ and its entrance region (Fig. 9). Positive anomalies are observed south of the AEJ and their extension is limited over the continent. The exit region of the jet which corresponds to the region where negative anomalies of zonal wind at 600 hPa appear (30°W–10°W)/10°N–25°N) is seen to coincide with the increased convection off the coast of West Africa (Fig. 6). The weak convective phase (phase 5) is characterised by strong negative anomalies south of the core of the jet and are mainly located over the Atlantic Ocean and the gulf of Guinea. However, positive anomalies of zonal

wind at 600 hPa are observed over the exit region during the weak convective phase (Fig. 6).

During the strong convective phase, the ensemble average of models' composites exhibits positive zonal wind anomalies at 600 hPa south of the AEJ core, which extend further into the Atlantic compared to the observations. Conversely, in the weak convection phase (phase 5) similar though opposite anomalies are simulated. Such westerly (easterly) anomalies south of the AEJ related to enhanced (weakened) convection over West Africa are consistent with the results from Omotosho and Abiodun (2007), who found that wet (dry) periods are associated with strong west to southwesterly (east to northeasterly) wind anomalies south of the AEJ, which could transport moisture away from the jet.

### 3.3 Mechanisms through which MJO impacts West Africa

Results so far presented have shown good evidence for the impact of the MJO on West African rainfall variability. Therefore, further investigations are carried out to analyse the physical mechanisms through which such impact takes place. Previous studies highlighted the roles of equatorial Kelvin and Rossby waves in MJO propagation (e.g. Matthews 2004; Mohino et al. 2012). Roundy and Frank (2004b) have highlighted the importance of westward-propagating equatorial Rossby modes interacting with the MJO in accounting for much of the intraseasonal convective variability within the tropics.
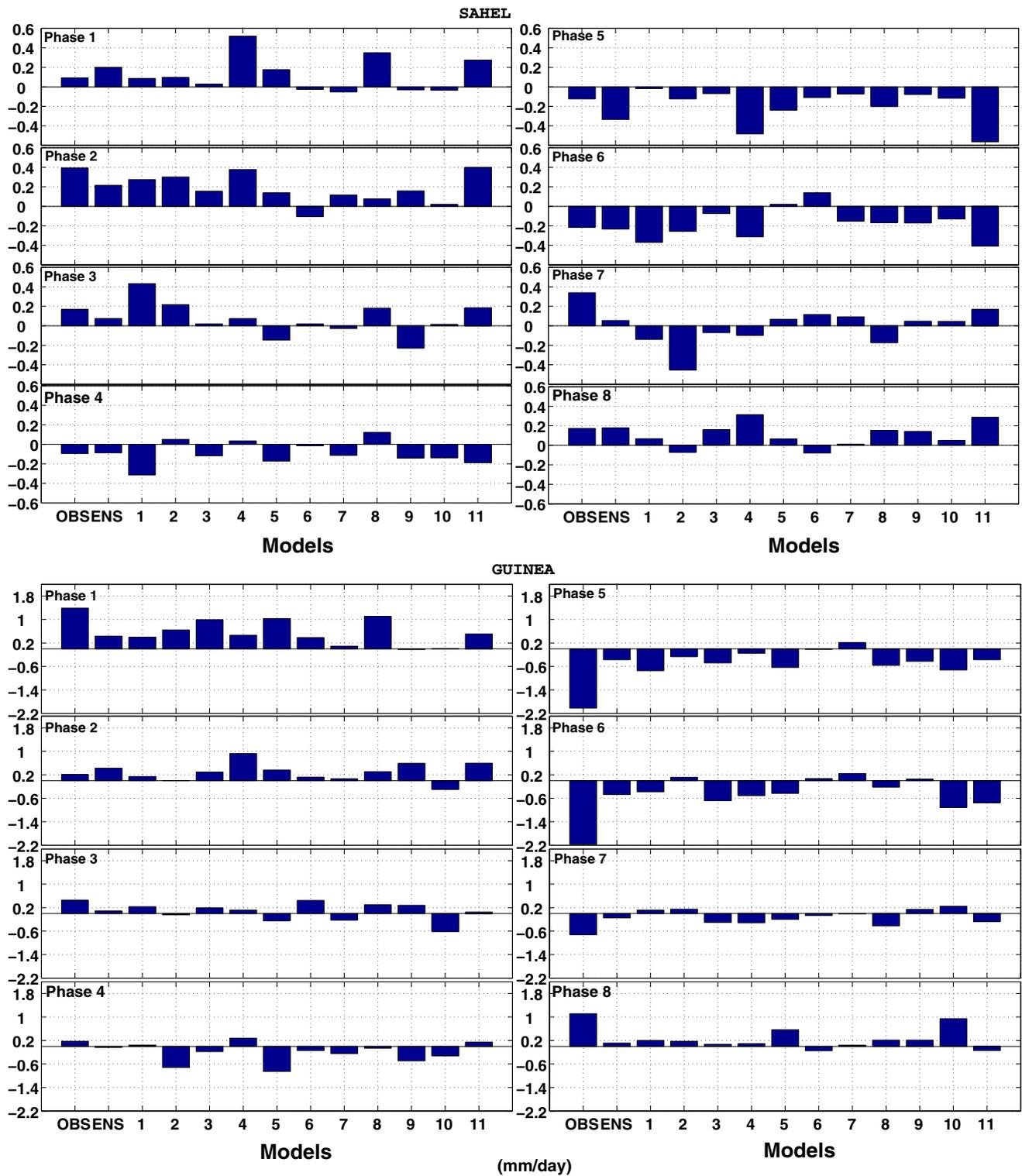
**Fig. 8** Composites of observed and simulated deseasonalized rainfall (mm/day) anomalies averaged over the Sahel (20°W–10°E and 10°N–20°N) and Guinean Coast (12°W–6°E and 4°N–7°N) boxes for each phase in the observations, models and the ensemble average of models' composites. The composites are averaged over the different boxes according to the different eight phases of MJO

**Fig. 9** Composites of zonal wind anomalies (m/s) at 600 hPa (*shaded*) during the strong (**a**, **c**) and weak (**b**, **d**) convective phases of MJO from the observations (**a**, **b**) and the ensemble average of models' composites (**c**, **d**) over West Africa. The *green contour lines* represent the climatological zonal wind at 600 hPa. The *crosses* mark the areas where at least eight (8) out of 11 models are consistent on the sign of the composite. *Grey contours* represent the area where the zonal wind anomalies at 600 hPa are 95 % significant according to a two-tailed *t* test
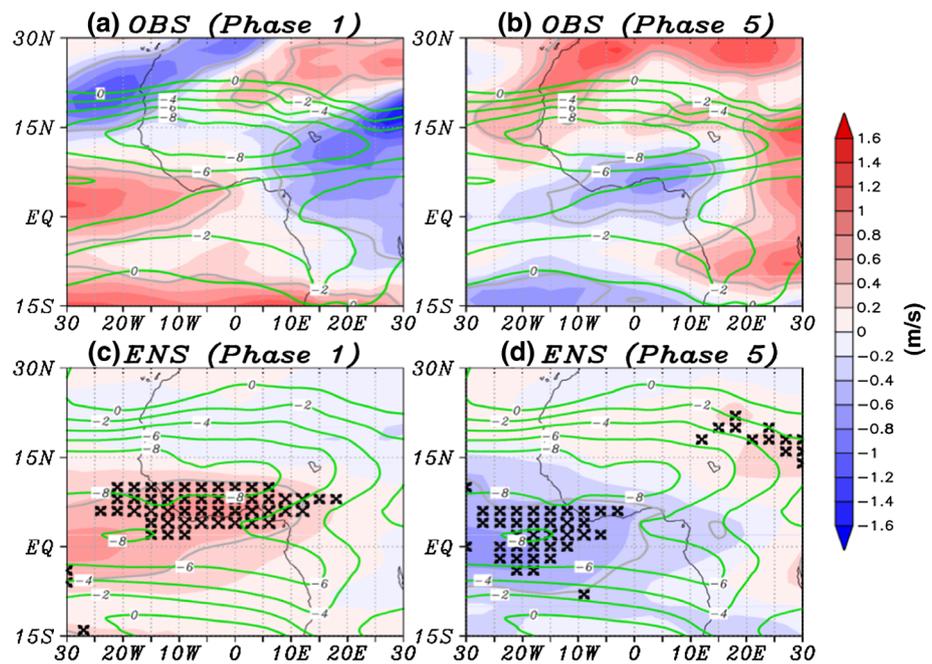


To investigate the role of these waves a composite hovmoller diagram of 850 hPa anomalies of zonal wind (shaded), OLR (contours in Fig. 10a, c) and SLP (contours in Fig. 10b, d) averaged over the latitude between 10°S and 10°N is presented for the observations (Fig. 10a, b) and for the ensemble average of models' composites (Fig. 10c, d). The observations show a clear eastward propagation of the OLR anomalies from the Indian Ocean to the western Pacific. The negative OLR anomalies (enhanced convection) are preceded by easterly winds at 850 hPa and followed by westerly ones. The opposite is found for positive OLR anomalies (reduced convection). The easterly propagating OLR anomalies weaken around 160°E. From that point, the propagation of zonal wind anomalies at 850 hPa is increased in speed to approximately 30 m/s, which is more consistent with a dry Kelvin wave (Milliff and Madden 1996; Wheeler and Kiladis 1999). In addition, beyond 120°E–150°E the negative zonal wind anomalies at 850 hPa are in phase with the negative sea level pressure ones, and vice versa, which is also suggestive of a dry Kelvin wave according to Sobel and Kim (2012). Thus, our results suggest that the enhanced (reduced) convection anomalies in the western Pacific would trigger a dry Kelvin wave that would propagate from these longitudes leading the perturbation eastward, consistently with previous works (Roundy 2012; Sobel and Kim 2012). Such dry Kelvin waves reach the South American coast where they seem to promote convection anomalies of the opposite sign to those that triggered the dry Kelvin waves in the Pacific Warm Pool. The speed of the propagation is reduced, the anomalies of zonal wind at 850 hPa and SLP weaken and

the phasing between both variables changes, suggesting that the dry Kelvin wave does not progress further east than 60°W.

Compared to the observations, the eastward propagation of the OLR anomalies (contours) is well simulated by the ensemble average of models' composites over the Indian Ocean and the West Pacific, though they show weaker anomalies (Fig. 10c).

The ensemble average of models' composites also shows a phasing between anomalies of zonal wind at 850 hPa and sea level pressure (contours) from 120°E-150°E to the east, suggesting also the emission of a dry Kelvin wave in the models (Fig. 10d), which would weaken once it arrives over South America. Sea level pressure anomalies are, nevertheless, much weaker in the simulation than in the observations, especially over Africa.

In order to split out the contribution of the different equatorial coupled waves on the overall impact a wavenumber frequency spectral analysis is performed. In Fig. 11 we highlight the spectral peaks by plotting the ratio of the power spectra above the background OLR spectrum (estimated as the OLR power spectrum smoothed several times in wavenumber and in frequency, see Wheeler and Kiladis 1999 for more details). The observations (Fig. 11a) show strong spectral content in the MJO band, at a frequency of around 0.025 cpd (period of approximately 40 days) for the range of eastward planetary wavenumber of 1 through to about 7. The eastward moving Kelvin waves occupy a broad region of the wavenumber–frequency regions in the 0.05–0.25 cpd band (periods of 4–20 days) (Wheeler and Kiladis 1999; Wheeler et al. 2000; Roundy and Frank
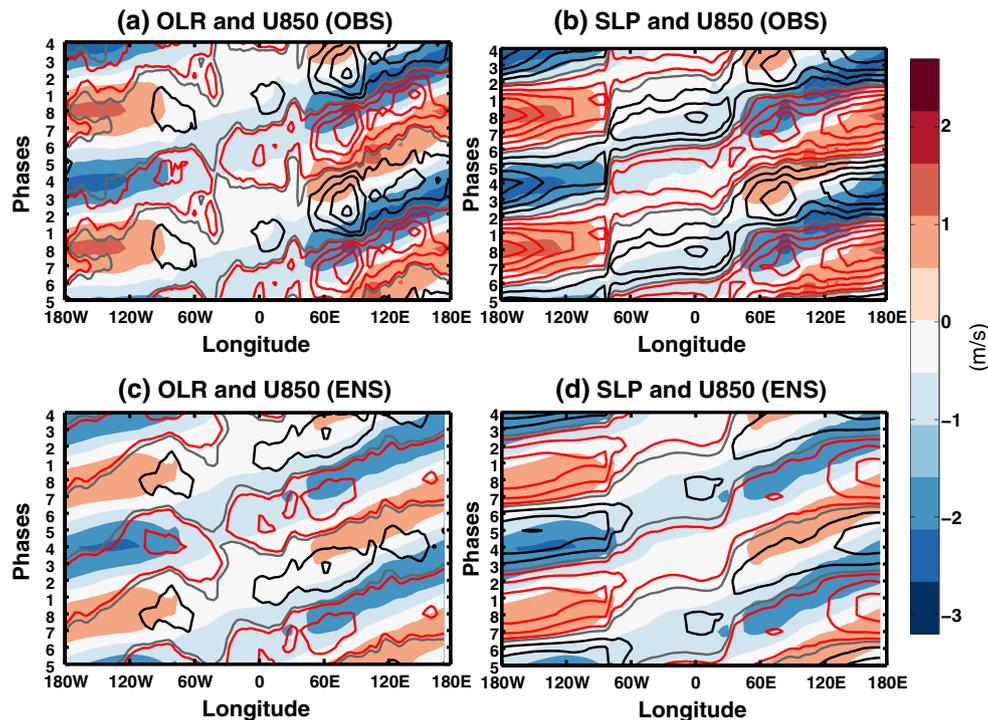
**Fig. 10** Hovmoller diagram performed over the composite of deseasonalized anomalies averaged between 10°S and 10°N of zonal wind at 850 hPa (m/s), OLR (W/m²) and SLP (hPa) for observations (**a**, **b**) and the average of composites (**c**, **d**). Wind anomalies are shaded. The *black solid contours* represent the negative anomalous values of OLR (SLP) while the *red solid contours* highlight the positive ones in **a** and **c** (**b**, **d**). The *grey lines* represent the contour zero for OLR (**a**, **c**) and SLP (**b**, **d**). The OLR values vary from −16 to 16 W/m² while SLP's contours are ranging from −1 to 1 hPa. The interval between *lines* is 4 W/m² for OLR values and 0.2 hPa for SLP's values

2004a) while westward Rossby waves exhibit a strong component of westward wavenumbers of 0–5 and a frequency similar to the one of the MJO. Additional analysis shows that the ensemble average of models' composites (Fig. 11b) simulates a strong signal in the MJO band at frequency around 0.025 cpd for the range of eastward planetary wavenumber of 1 through to about 7. Nevertheless, it shows that the ensemble average of AMIP simulations exhibits a very weak peak in the Kelvin wavenumber frequency zone compared to the observations. The spectral peak simulated by the ensemble average of models' spectra in the region of Rossby waves is stronger than the observed one. The same analysis is performed also for each individual model and they mostly show a pattern similar to the observed one for MJO and Rossby components. However, only the BCC-CSM1-1 and BCC-CSM1-1-M models show a clear spectral component in the region corresponding to the convectively coupled Kelvin waves (Figure S7–S12).

To further analyse the skill of each model in representing the symmetric component of the different equatorially trapped waves we present in Fig. 12a the ratio of the power spectra to the background power spectrum intensity averaged over the two different boxes (red and black boxes presented in Fig. 11) that represent the eastward and

westward propagating convectively coupled waves. The ensemble average of models' composites is calculated by averaging over the different models taken individually. The observations show the maximum OLR power contribution in the eastward propagating (MJO) box, followed by the westward propagating (Rossby) component. Models tend to underestimate the power spectrum corresponding to the eastward component peaks and overestimate the one in the westward box. In our sample of 11 models, only three (NorESM1-M, BCC-CSM1-1 and BCC-CSM1-1-M) show an average of OLR power in the eastward box above 1.4 times the background spectrum (the approximate content shown by the observations). In addition, and conversely to the observed behaviour (the same westward and eastward boxes), the models show an average spectrum in the westward box above the one in the eastward box, except for the BCC-CSM1-1 model.

In order to separate the role played by the different propagating waves in the convection signal obtained over West Africa we repeat the composite procedure with OLR fields that are previously filtered for the westward and eastward regions (defined in Fig. 11) of the wavenumber–frequency spectral content. We leave out the convectively Kelvin wave component from this analysis because our definition

**Fig. 11** Wavenumber frequency spectral analysis of OLR data from the observations (**a**) and the ensemble average of models spectra (**b**). The eastward part of the signal (MJO) is extracted from 0 to 9 (see *black box*) of the periods of roughly 30–90 days and the westward part (corresponding to the Rossby waves) is extracted from −10 to 1 (see *red box*). The units are the ratio of the power spectra above the background OLR spectrum obtained after smoothing several times in wavenumber and in frequency
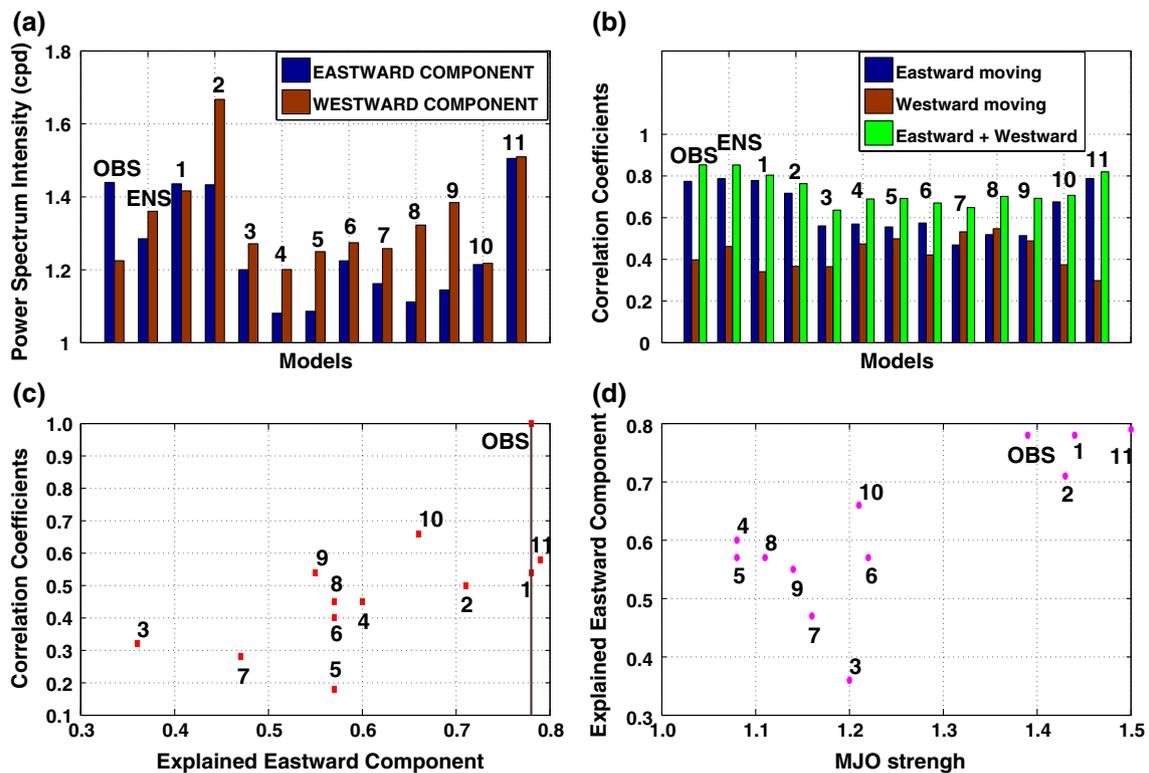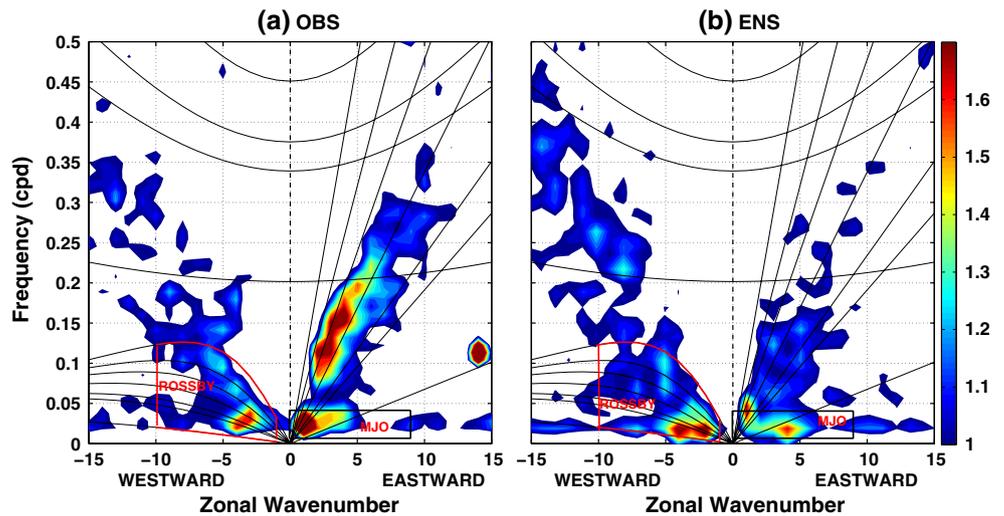




**Fig. 12 a** Observed and simulated spectrum intensity above the background averaged over the different equatorial waves boxes (eastward and westward component) defined in Fig. 11. **b** Spatial correlation in the tropics between MJO composites of unfiltered OLR and filtered OLR fields using the eastward and westward boxes defined in Fig. 11. **c** Scatterplot between the correlation coefficients between the observations and each of AMIP's models in the tropics and the composites of deseasonalized OLR filtered over MJO's wavenumber–frequency box. The *brown line* in **c** delimits the observed value of the composites of deseasonalized OLR filtered over MJO's wavenumber–frequency box. **d** Scatterplot between the strength of MJO and the composites of deseasonalized OLR filtered over MJO's wavenumber–frequency box

of the MJO signal, which is based on fields filtered in the 20–90 day band (0.011–0.05 cpd), is effectively filtering out those waves with a frequency higher than 0.05 cpd

(periods lower than 20 days). This methodology can then only separate the westward propagating component, which we have identified as the convectively coupled Rossby

wave, and the eastward propagating component, which we have identified with the MJO. We can not rule out that some convectively coupled Kelvin waves with very low frequencies (lower than 0.05 cpd) and equivalent depths from 8 to 90 m could be included in the eastward propagating signature.

In addition, we represent in Fig. 12b the correlation between the composite of unfiltered and filtered OLR fields taking into account the entire tropics between 15°S–15°N and all eight phases of MJO. In the observations, the main contribution to the MJO tropical signal shown in Fig. 4a comes from the eastward propagating signal or MJO (correlation between the original composite and the one obtained when filtering in the MJO area of the wavenumber–frequency spectral content is 0.78). However, there is also a contribution from the westward propagating signal we have termed convectively coupled Rossby waves (correlation of 0.40) and both together explain a higher percentage of the tropical convection signal (correlation of 0.85). In the models, the spatial correlation between the overall signal and the one coming from the eastward propagating part tend be lower than for the observations, ranging from 0.47 to 0.78 (Fig. 12b). Such correlation tends to be higher for those models with a stronger spectral peak in the MJO region (Fig. 12d). In addition, the higher the dominance of the eastward propagating signal in the modelled composite, the likelier a better resemblance of the simulated tropical signal with the observed composite (Fig. 12c). The correlation between the overall signal and the part coming from the westward propagating signal tends to be higher in the models than in the observations, with 7 models out of 11 (IPSL-CM5A-LR, IPSL-CM5A-MR, MPI-ESM-MR, HadGEM2-A, CNRM-CM5, IPSL-CM5A-MR and MPI-ESM-LR) showing a correlation higher than 0.40. In most models the overall MJO signal is dominated by the eastward propagating component, as in the observations (Fig. 12a). When the OLR fields are filtered using both the eastward and westward propagating components of the spectra, the correlations are higher than when using only one of both components (Fig. 12a). These results suggest that the westward equatorial Rossby waves are also important to explain the overall impact of the MJO over West Africa, in accordance with previous studies (Roundy and Frank 2004b; Mohino et al. 2012).

## 4 Conclusions

This research study was conducted using a set of simulations from AMIP experiments to investigate the relationship between MJO and the West African monsoon during the boreal summer and also to assess the performance of the models in simulating such link. The study evaluated the

impact of the MJO on convection and rainfall in the region and investigated the dynamical processes involved.

Our results show that the AMIP-type simulations from the 11 models we have analysed are able to simulate an eastward propagating signal in the tropics linking a barotropic wavenumber 1 structure in zonal winds with anomalies in convection. Such structure can account for a relevant part of the models intraseasonal variability (between 17.7 to 32.6 %, depending on the models) in the 20–90 day band, which is in all cases smaller than for the observations (37.6 %). We have identified such structure with the MJO and we have further research into its signature in convection in the tropics with a special focus on West Africa. The speed of propagation of such MJO in the models (from 36 to 39 days to complete a whole cycle) is close to the observed one (38.4 days to complete a cycle).

Regarding its impacts over West Africa, we have shown that, in accordance with the observations, the models tend to show two distinct phases with strong and weak convection, respectively, which are, in turn, connected to positive and negative rainfall anomalies, especially over the Gulf of Guinea, suggesting that the MJO can impact West African rainfall intraseasonal variability during the summer period. In general, the pattern of impact of the MJO signal on convection over West Africa is simulated by most of the models. However, the big challenge is the large variability of rainfall over West Africa. The MJO-West Africa relationship is further confirmed by the link between the MJO disturbances and the AEJ anomalies, particularly over the coastal regions. The analysis shows that the strong convective phase of the MJO is associated with a more eastward location of the AEJ and with positive anomalies located south of the jet. Conversely, the AEJ is weaker in the weak convection phase, with strong anomalies south of the jet. This relationship is well represented by the ensemble average.

The present study also found that the observed time lag between the positive/negative convection anomalies over the Indian Ocean and West Africa is about 15–20 days. That time lag correlation is well simulated by some models (NorESM1-M, MPI-ESM-MR, BCC-CSM1-1, IPSL-ESM-LR and CNRM-CM5) while others show longer values ranging from 20 to 25 days.

Regarding the mechanisms, our study suggests that the main impact of the MJO over West Africa is due to the eastward propagating part of the signal. Most of the tropical convection pattern can be obtained with just this component. However, we have also shown that the westward equatorial Rossby waves play a relevant role both in models and in the observations in the overall impact on convection over West Africa, in agreement with the work of Mohino et al. (2012). The simulations also show that the contrast between the Indian Ocean and West Africa in terms of the anomalous convection might be used as a

potential predictor since the results show a time lag of about 15–20 and/or 20–25 days between the two regions. The AMIP simulations suggest then a potential to predict occurrences of wet and dry sequences over West Africa if the MJO can be realistically predicted (Waliser et al. 1999; Jones et al. 2004b).

# References

Barlow M, Wheeler M, Lyon B, Cullen H (2005) Modulation of daily precipitation over southwest Asia by the Madden–Julian oscillation. Mon Weather Rev 133:3579–3594

Bond NA, Vecchi GA (2003) The influence of the Madden–Julian oscillation (MJO) on precipitation in Oregon and Washington. Weather Forecast 18(4):600–613

Carvalho L, Jones C, Liebmann B (2004) The South Atlantic convergence zone: intensity, form, persistence, and relationships with intraseasonal to interannual activity and extreme rainfall. J Clim 17:88–108

CLIVAR Madden-Julian Oscillation Working Group (2009) MJO simulation diagnostics. J Clim 22:3006–3030. doi:10.1175/2008JCLI2731.1

Crueger T, Stevens B, Brokopf R (2013) The Madden–Julian oscillation in ECHAM6 and the introduction of an objective MJO metric. J Clim 26:3241–3257. doi:10.1175/JCLI-D-12-00413.1

Dee DP, Uppala SM, Simmons AJ, Berrisford P, Poli P, Kobayashi S, Andrae U, Balmaseda MA, Balsamo G, Bauer P, Bechtold P, Beljaars ACM, van de Berg L, Bidlot J, Bormann N, Delsol C, Dragani R, Fuentes M, Geer AJ, Haimberger L, Healy SB, Hersbach H, Hólm EV, Isaksen L, Kållberg P, Köhler M, Matricardi M, McNally AP, Monge-Sanz BM, Morcrette J-J, Park B-K, Peubey C, de Rosnay P, Tavolato C, Thépaut J-N, Vitart F (2011) The ERA-Interim reanalysis: configuration and performance of the data assimilation system. Q J R Meteorol Soc 137:553–597. doi:10.1002/qj.828

Donald A et al (2006) Near-global impact of the Madden–Julian oscillation on rainfall. Geophys Res Lett 33:L09704. doi:10.1029/2005GL025155

Gadgil S, Rao PRS (2000) Farming strategies for a variable climate—a challenge. Curr Sci 78:1203–1215

Guilyardi E, Wittenberg A, Fedorov A, Collins M, Wang C, Capotondi A, van Oldenborgh GJ, Stockdale T (2009) Understanding El Nino in ocean–atmosphere general circulation models: progress and challenges. Bull Am Meteorol Soc 90:325–340

Hayashi Y (1982) Space–time spectral analysis and its applications to atmospheric waves. J Oceanogr Soc Jpn 60:156–171

Hendon HH, Zhang CD, Glick JD (1999) Interannual variation of the Madden–Julian oscillation during austral summer. J Clim 12:2538–2550

Higgins W, Schemm J, Shi W, Leetmaa A (2000) Extreme precipitation events in the western United States related to tropical forcing. J Clim 13:793–820

Huffman GJ, Adler RF, Morrissey MM, Bolvin DT, Curtis S, Joyce R, McGavock B, Susskind J (2001) Global precipitation at one-degree daily resolution from multisatellite observations. J Hydrometeorol 2:36–50

Hung MP, Lin JL, Wang W, Kim D, Shinoda T, Weaver SJ (2013) MJO and convectively coupled equatorial waves simulated by CMIP5 climate models. J Clim 26:6185–6214. doi:10.1175/JCLI-D-12-00541.1

Janicot S, Sultan J (2001) Intra-seasonal modulation of convection in the West African monsoon. Geophys Res Lett 28:523–526

Janicot S, Mounier F, Gervois S, Hall JN, Leroux S, Sultan B, Kiladis GN (2009) The dynamics of the West African monsoon. Part IV: analysis 25–90-day variability of convection and the role of the Indian monsoon. J Clim 22:1541–1565. doi:10.1175/2008JCLI2314.1

Jones C, Schemm JE (2000) The influence of intraseasonal variations on medium-to extended-range weather forecasts over South America. Mon Weather Rev 128:486–494

Jones C, Waliser DE, Lau WK, Stern W (2000) Prediction skill of the Madden and Julian oscillation in dynamical extended range forecasts. Clim Dyn 16:273–289

Jones C, Waliser DE, Lau WK, Stern W (2004a) The Madden–Julian oscillation and its impact on Northern Hemisphere weather predictability. Mon Weather Rev 132:1462–1471

Jones C, Carvalho LMV, Higgins RW et al (2004b) Statistical forecast skill of tropical intraseasonal convective anomalies. J Clim 17:2078–2095

Kessler WS (2001) EOF representations of the Madden–Julian oscillation and its connection with ENSO. J Clim 14:3055–3061

Kim D, Sperber K, Stern W, Waliser D, Kang IS, Maloney E, Schubert S, Wang W, Weickmann K, Benedict J, Khairoutdinov M, Lee MI, Neale R, Suarez M, ThayerCalder K, Zhang G (2009) Application of MJO simulation diagnostics to climate models. J Clim 22:6413–6436

Knutson T, Weickmann K (1987) 30-60 day atmospheric oscillations: composite life cycles of convection and circulation anomalies. Mon Weather Rev 115:1407–1436

Lavender SL, Matthews AJ (2009) Response of the West African monsoon to the Madden–Julian oscillation. J Clim 22:4097–4116

Liebmann B, Smith CA (1996) Description of a complete (interpolated) outgoing longwave radiation dataset. Bull Am Meteorol Soc 77:1275–1277

Liebmann B, Hendon HH, Glick JD (1994) The relationship between tropical cyclones of the western Pacific and Indian Oceans and the Madden–Julian oscillation. J Meteorol Soc Jpn 72:401–411

Liebmann B, Kiladis GN, Vera CS, Saulo AC, Carvalho LMV (2004) Subseasonal variations of rainfall in South America in the vicinity of the low-level jet east of the Andes and comparison to those in the South Atlantic convergence zone. J Clim 17:3829–3842

Lin JL, Kiladis GN, Mapes BE, Weickmann KM, Sperber KR, Lin W, Wheeler MC, Schubert SD, Del Genio A, Donner LJ, Emori S, Gueremy JF, Hourdin F, Rasch PJ, Roeckner E, Scinocca JF (2006) Tropical intraseasonal variability in 14 IPCC AR4 climate models: part I: convective signals. J Clim 19:2665–2690. doi:10.1175/JCLI3735.1

Madden RA, Julian PR (1971) Description of a 40–50 day oscillation in the zonal wind in the tropical Pacific. J Atmos Sci 28:702–708

Madden RA, Julian PR (1994) Detection of a 40–50 day oscillation in the zonal wind in the tropical Pacific. Mon Weather Rev 122:813–837

Maloney E, Hartmann D (2000) Modulation of eastern North Pacific hurricanes by the Madden–Julian oscillation. J Clim 13:1451–1460

Maloney E, Shaman J (2008) Intraseasonal variability of the West African monsoon and Atlantic ITCZ. J Clim 12:2898–2918

Matthews A (2004) Intraseasonal variability over the tropical Africa during northern summer. J Clim 17:2427–2440

Mauritsen T et al (2012) Tuning the climate of a global model. J Adv Model Earth Syst 4:M00A01. doi:10.1029/2012MS000154

Milliff RF, Madden RA (1996) The existence and vertical structure of fast, eastward-moving disturbances in the equatorial troposphere. J Atmos Sci 53:586–597

Mohino E, Janicot S, Douville H, Li ZXL (2012) Impact of the Indian part of the summer MJO on West Africa using nudged climate simulations. Clim Dyn 38:2319–2334. doi:10.1007/s00382-011-1206-y

Mounier F, Janicot S (2004) Evidence of two independent modes of convection at intraseasonal timescale in the West African summer monsoon. Geophys Res Lett 31:L16116. doi:10.1029/2004GL020665

Mounier F, Kiladis GN, Janicot S (2007) Analysis of the dominant mode of convectively coupled Kelvin waves in the West African monsoon. J Clim 20:1487–1503

North GR, Bell TL, Cahalan RF (1982) Sampling errors in the estimation of empirical orthogonal functions. Mon Weather Rev 110:699–706

Omotosho JB, Abiodun BJ (2007) A numerical study of moisture build-up and rainfall over West Africa. Meteorol Appl 14(3):209–225

Pohl B, Janicot S, Fontaine B, Marteau R (2009) Implication of the Madden–Julian oscillation in the 40-day variability of the West African monsoon. J Clim 22:3769–3785

Randall DA et al (2007) Climate models and their evaluation. Climate change 2007: the physical science basis. In: Solomon S et al (eds) Contribution of working group I to the fourth assessment report of the intergovernmental panel on climate change. Cambridge University Press, Cambridge, pp 589–662

Roundy PE (2012) Observed structure of convectively coupled waves as a function of equivalent depth: Kelvin waves and the Madden–Julian oscillation. J Atmos Sci 69:2097–2106. doi:10.1175/JAS-D-12-03.1

Roundy PE, Frank WM (2004a) A climatology of waves in the equatorial region. J Atmos Sci 61:2105–2132

Roundy PE, Frank WM (2004b) Effects of low-frequency wave interactions on intraseasonal oscillations. J Atmos Sci 61:3025–3040

Slingo JM et al (1996) Intraseasonal oscillation in 15 atmospheric general circulation models: results from an AMIP diagnostic subproject. Clim Dyn 12:325–357

Sobel AH, Kim D (2012) The MJO–Kelvin wave transition. Geophys Res Lett 39(L20808):2012G. doi:10.1029/L053380

Sultan B, Janicot S, Diedhiou A (2003) The West African monsoon dynamics. Part I: documentation of intraseasonal variability. J Clim 16:3390–3406

Sultan B, Baron C, Dingkuhn M, Sarr B, Janicot S (2005) Agricultural impacts of large-scale variability of the West African monsoon. Agric For Meteorol 128:93–110

Taylor KE, Stouffer RJ, Meehl GA (2012) An overview of CMIP5 and the experiment design. Bull Am Meteorol Soc 93:485–498. doi:10.1175/BAMS-D-11-00094.1

Venegas SA (2001) Statistical methods for signal detection in climate. Danish Center for Earth System Science

Ventrice MJ, Thorncroft CD, Roundy PE (2011) The Madden Julian's oscillation on African easterly waves and downstream tropical cyclogenesis. Mon Weather Rev 139:2704–2722

Waliser DE, Lau KM, Kim JH (1999) The influence of coupled sea surface temperatures on the Madden–Julian oscillation: a model perturbation experiment. J Atmos Sci 56:333–358

Waliser DE et al (2003) AGCM simulations of intraseasonal variability associated with the Asian summer monsoon. Clim Dyn 21:423–446

Wang W, Schlesinger ME (1999) The dependence on convective parameterization of the tropical intraseasonal oscillation simulated by the UIUC 11-layer atmospheric GCM. J Clim 12:1423–1457

Wheeler M, Hendon H (2004) An all-season real-time multivariate MJO index: development of an index for monitoring and prediction. Mon Weather Rev 132:1917–1932

Wheeler M, Kiladis GN (1999) Convectively coupled equatorial waves: analysis of clouds and temperature in the wavenumber–frequency domain. J Atmos Sci 56:374–399

Wheeler MC, McBride JL (2005) Australian–Indonesian monsoon. In: Lau WKM, Waliser DE (eds) Intraseasonal variability of the atmosphere–ocean climate system. Praxis Publishing, Chichester, p 436

Wheeler M, Kiladis GN, Webster PJ (2000) Large-scale dynamical fields associated with convectively coupled equatorial waves. J Atmos Sci 57:613–640

Yasunari T (1979) Cloudiness fluctuations associated with the northern hemisphere summer monsoon. J Meteorol Soc Jpn 57:227–242

Zhang CD (2005) Madden–Julian oscillation. Rev Geophys 43(RG2003):2004R. doi:10.1029/G000158

Zhang C, Dong M, Gualdi S, Hendon HH, Maloney ED, Marshall A, And Sperber KR, Wang W (2006) Simulations of the Madden–Julian oscillation in four pairs of coupled and uncoupled global models. Clim Dyn 27:573–592. doi:10.1007/s00382-006-0148-2